https://doi.org/10.5194/egusphere-2026-3333
Preprint. Discussion started: 30 June 2026

# Refined CT-Based Proxy for Foraminiferal Diagenesis Shows Evidence for Shallow Dissolution in North Atlantic Sediment Cores.

Thomas L. Weiss[1,2,3]; Alessio Fabbrini[1]; Jerry F. McManus[4,5]; Elwyn de la Vega[1]; Hridya Krishnakumar[1]; Audrey Morley[1,2]

[1]University of Galway, School of Geography, Archaeology, and Irish Studies, Galway, Ireland

[2]iCRAG—Irish Centre for Research in Applied Geosciences, Belfield, Dublin 4, Ireland

[3]Georgia Institute of Technology, Atlanta, GA 30332 USA

[4]Lamont-Doherty Earth Observatory, Columbia University, Palisades, NY 10964, USA

[5]Department of Earth and Environmental Sciences, Columbia University, New York, NY 10027, USA

*Corresponding authors: Thomas Weiss (tweiss9@gatech.edu) and Audrey Morley (audrey.morley@universityofgalway.ie)*

**Abstract:** Geochemical reconstructions (e.g., $\delta^{18}O$, Mg/Ca) derived from the shells of the polar and subpolar planktonic foraminifera *Neogloboquadrina pachyderma* and *Neogloboquadrina incompta* are foundational to our understanding of high-latitude climate history. However, these species are highly vulnerable to diagenetic alteration—specifically partial dissolution and secondary calcification—which can significantly bias paleoceanographic signals. We introduce nCTDX%, a refined X-ray micro-computed tomography (µCT) proxy designed to quantify foraminiferal diagenesis with increased objectivity and time efficiency. By implementing mathematical thresholding and normalization to a density standard, nCTDX% allows for the direct comparison of shell density across different scans and study sites. Our results from North Atlantic, Nordic Sea, and North Pacific sediment cores confirm that both species dissolve from the inside out, preferentially removing internal structures previously shown to be rich in Mg and leaving behind resistant, low-Mg gametogenic crusts. While core-top nCTDX% correlates with bottom-water carbonate saturation ($\Delta[CO_3^{2-}]$), we demonstrate that undersaturated pore waters can initiate significant dissolution within the top 2 cm of the sediment column, even at locations where overlying bottom waters are supersaturated. Furthermore, we show that nCTDX% is a sensitive indicator of secondary inorganic overgrowth, which appears in SEM images as low-density rhombohedral crystals on shell exteriors. The potential for pore water dissolution and inorganic calcification to overprint the bottom water $\Delta[CO_3^{2-}]$ signal contained in nCTDX% and other µCT and dissolution-based proxies suggests extreme caution must be taken when they are applied as proxies for bottom water carbonate ion saturation. Instead, given that even partial dissolution of internal shell walls can bias reconstructed temperatures by 1–2°C, our findings suggest that µCT and dissolution-based proxies are better utilized as indicators of in situ diagenetic state. We therefore advocate for the routine application of nCTDX% to evaluate the preservation state of downcore samples and ensure the fidelity of geochemical paleoclimate records.

## 1.Introduction

Reconstructions of past ocean climate variables generated from geochemical proxies (e.g., $\delta^{18}O$, $\delta^{13}C$, Mg/Ca, $\delta^{11}B$, etc.) measured from the shells of planktonic foraminifera are foundational to our understanding of earth's climate history. However, foraminifera shells are vulnerable to diagenesis from the moment they die and begin their decent to the seafloor (Chanda et al., 2019; Zeebe and Wolf-Gladrow, 2001). For example, when shells are exposed to water undersaturated in carbonate ion ($\Delta[CO_3^{2-}] = [CO_3^{2-}]_{in\ situ} - [CO_3^{2-}]_{saturation}$), they begin to partially dissolve. Critically, foraminiferal shell solubility and geochemistry are heterogeneous, and as a result, partial dissolution poses a significant risk of biasing geochemical-based paleoclimate reconstructions (Bauch et al., 1997; Brown and Elderfield, 1996; Davis et al., 2017; Iwasaki et al., 2023; Johnstone et al., 2010; Jonkers et al., 2016; Kozdon et al., 2009; Lohmann, 1995). This is particularly relevant for species such as *Neogloboquadrina pachyderma* and *Neogloboquadrina incompta* that form thick outer gametogenic crusts that are low in Mg/Ca and high in $\delta^{18}O$ relative to the inner ontogenetic calcite (Bauch et al., 1997; Davis et al., 2017; Hupp and Fehrenbacher, 2023; Jonkers et al., 2016; Kozdon et al., 2009; Westgård et al., 2026).

*Neogloboquadrina pachyderma* is the only planktonic foraminifera living in surface waters with mean annual temperature below 4° C (Bertlich et al., 2021; Kucera, 2007; Lombard et al., 2009; Manno et al., 2012; Spindler and Dieckmann, 1986; Westgård et al., 2023; Zamelczyk et al., 2021) and thus constitutes 96-99% of the Arctic and Polar species assemblage (Husum and Hald, 2012). Therefore, assessing the impact of diagenetic processes including dissolution for this species and their impact on shell geochemistry is critical if we aim to accurately reconstruct past climate histories for Arctic and Polar Oceans (Bauch et al., 1997; Bauch et al. 2003; Morley et al., 2024). Although it is not as resilient to low temperatures as *N. pachyderma*, *N. incompta* also occupies a wide range of subpolar environments that are important to paleoclimate reconstructions (Kucera, 2007).

Foraminifera shells are at greatest risk of dissolution at core sites where the sea floor is located below the lysocline where deep ocean waters are undersaturated in carbonate ion (Zeebe and Wolf-Gladrow, 2001). Consequently, to avoid the risks of partial dissolution, most geochemistry-based foraminiferal paleoceanographic records are generated from sediment cores collected above the lysocline, in bottom waters supersaturated in dissolved carbonate ion (Brown and Elderfield, 1996). This approach, however, does not necessarily avoid partial dissolution as there is no guarantee that bottom waters were supersaturated in carbonate ion in the past. Furthermore, the release of $CO_2$ via respiration of organic matter deposited in sediments that is often focused in the top 5-10 cm of the sediment column can leave the interstitial pore waters undersaturated in carbonate ion to sediment depths >35cm even if overlying bottom waters are saturated (Archer et al., 2000; Archer and Maier-Reimer, 1994; Cetiner et al., 2025; Emerson and Bender, 1981; Martin and Sayles, 1996). Given the difficulty of measuring pore water carbonate chemistry, most paleoceanographic studies rely solely on modern bottom water $\Delta[CO_3^{2-}]$ and reconstructions of its past variability to assess the potential of partial dissolution impacting downcore shell chemistry, ignoring pore water $\Delta[CO_3^{2-}]$.

In addition to partial dissolution, water supersaturated in $[CO_3^{2-}]$ can also result in diagenesis that influences shell geochemistry. For example, foraminifera specimens collected from carbonate mounds where bottom waters are supersaturated in carbonate ion can exhibit inorganic overgrowth of rhombohedral calcite crystals (Boussetta et al., 2011; Hoogakker et al., 2009; Morley et al., 2017; Reuning et al., 2005; van Raden et al., 2011) that have aberrantly high Mg/Ca values (Morley et al., 2017). Furthermore, inorganic overgrowth can occur within the sediment column, where the dissolution of carbonates leads to supersaturated pore waters (Cetiner et al., 2025).

A common method for identifying diagenesis is by Scanning Electron Microscopy (SEM) (Boussetta et al., 2011; Jong et al., 2026; Morley et al., 2017; van Raden et al., 2011). However, this method isn't quantitative and does

https://doi.org/10.5194/egusphere-2026-3333
Preprint. Discussion started: 30 June 2026

not always detect dissolution or secondary calcification. Alternatively, foraminiferal shell weight (Anand et al., 2003; Boyle, 1988; Petit et al. 1999; Russell et al., 2004), size normalized shell weight (Boyle, 1988; Broecker and Clark, 2001; Henehan et al., 2017; Petit et al. 1999; Russell et al., 2004), and shell fragmentation (Berger, 1970; Le and Shackleton, 1992; Thunell, 1976) have been applied as proxies for past bottom water carbonate ion saturation and foraminiferal shell dissolution. While useful, many of these methods have potential secondary constraints such as surface water productivity, variations in original shell size or density, and pore water dissolution (Henehan et al., 2017; Yu and Elderfield, 2007; Zarkogiannis et al., 2022), and none directly identify primary dissolution structures.

Instead, X-ray micro-computed tomography (micro-CT) is an emerging and powerful tool for inferring dissolution in planktonic foraminifera because it produces high-resolution 3D density models from foraminiferal shells. CT-number histograms representing density relative to a standard can then be used to generate quantitative metrics such as the *% low-CT-number calcite volume* (CTDX%) (De Araújo et al., 2025; Iwasaki et al., 2015; Iwasaki et al., 2019a; Iwasaki et al., 2019b; Iwasaki et al., 2022; Jana et al., 2024; Johnstone et al., 2010; Johnstone et al., 2011; Johnstone et al., 2014; Zarkogiannis et al., 2022). For example, in a series of dissolution experiments and studies based on core top sediments, Iwasaki et al. (2015; 2019a; 2019b; 2022; 2023) demonstrated that µCT scans can be used to directly identify dissolution structures in foraminifera shells. They were then able to link high CTDX% derived from several tropical and midlatitude planktonic foraminifera species with low bottom water $\Delta[CO_3^{2-}]$ (Iwasaki et al., 2023). They concluded that CTDX% can be applied downcore as a proxy for past bottom water carbonate ion saturation, an important metric to assess carbon cycle processes in response to changing climates (Iwasaki et al., 2022; Iwasaki et al. 2023). However, unless it can be ruled out using complementary proxies (e.g., Iwasaki et al. 2022; Johnstone et al. 2014), the proposed approach and application downcore assumes that dissolution occurs only in bottom and not in pore waters. Furthermore, CTDX% has never been applied in locations where supersaturated bottom and pore waters are known to drive secondary inorganic calcification – a process known to reduce foraminiferal bulk density (Edgar et al., 2015; Roza-Llera et al., 2024). Secondary inorganic calcification and pore water dissolution therefore have the potential to increase CTDX% thereby resulting in misleadingly low bottom water $\Delta[CO_3^{2-}]$ when the proxy is applied down core to past climates.

In addition to these potential complications, we see several opportunities for refinement of the CTDX% proxy. First, the processing of µCT images for CTDX%, requires the user to distinguish between sediments contained within the shell and dissolved shell material to remove contaminants (Iwasaki et al., 2023). This process can be subjective and extremely time intensive especially when specimens are heavily dissolved and the line between altered shell and trapped sediments blurs (Johnstone et al., 2010). Second, once images are processed, endpoints of the raw intensity profile are visually chosen and then assigned normalized intensities of 0 and 100 before calculating CTDX% (Iwasaki et al., 2023). As a result, normalization to a density standard is removed, and pixel intensity cannot be compared across specimens to determine their relative density. Therefore, two specimens with the same intensity distribution shape, but different absolute densities could have the same CTDX%.

Here we use *N. pachyderma* and *N. incompta* specimens collected from Nordic Sea, North Pacific, and subpolar North Atlantic sediment cores to further develop the µCT-based proxy for diagenesis. Specifically, we aim to investigate the impacts of both undersaturated and supersaturated bottom and pore waters on the micro-CT proxy. We first refine image processing to minimize subjectivity. Second, we ensure normalization to a density standard to allow for comparison of normalized intensities across scans. We then apply our new method to *N. pachyderma* and *N. incompta* specimens and evaluate if our new proxy can robustly infer dissolution (remineralization) resulting from under- (super-) saturated bottom and porewater $\Delta[CO_3^{2-}]$. Lastly, to verify our approach, we generate SEM images of selected specimens for visual evaluation.

## 2. Methods

### 2.1 Sample collection

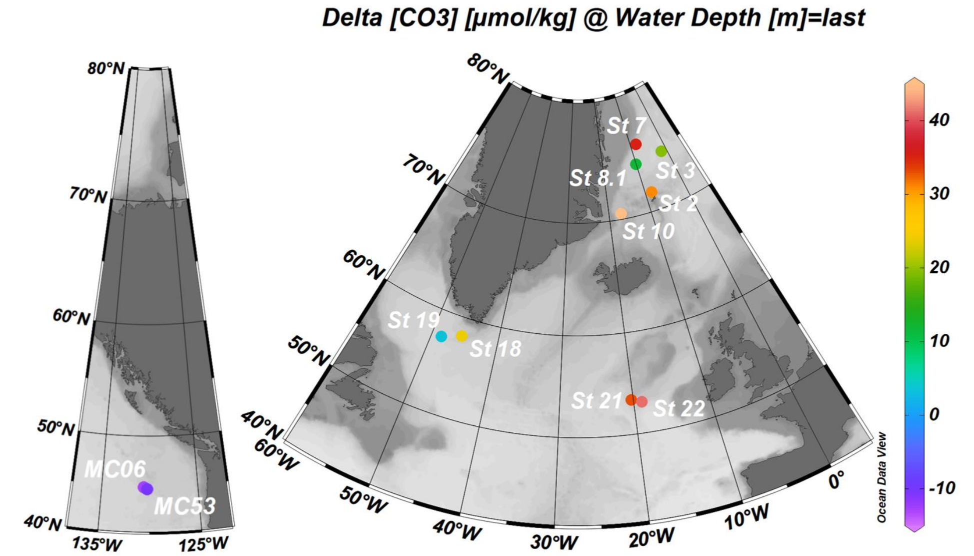

**Figure 1—CE23011, AT26-19, and GLODAP station locations and bottom water $\Delta[CO_3^{2-}]$. North Atlantic and Nordic Sea CE23011 bottom water $\Delta[CO_3^{2-}]$ was generated from CTD total alkalinity and DIC. North Pacific AT26-19 (white symbols) bottom water $\Delta[CO_3^{2-}]$ is calculated from GLODAPv2.2023 total alkalinity and DIC data from the six nearest stations. GLODAPv2.2023 data courtesy of the Global Ocean Data Analysis Project (https://www.glodap.info).**

North Atlantic and Nordic Sea sediment, porewater, and seawater samples were collected via multicore and CTD across 10 stations during the *RV Celtic Explorer* cruise CE23011 from 21 July to 20 August 2023 (Fig. 1 and Table 1). Water column samples for carbonate chemistry were collected via CTD Niskin bottles. Water column samples for alkalinity were analyzed onboard, while samples for dissolved inorganic carbon (DIC) were immediately poisoned with 200 µL of mercuric chloride per 500 mL of seawater and refrigerated until analysis on shore (see Sect. 2.2). Porewaters were extracted from predrilled multicores using Rhizons attached to 50 mL luer-lock syringes. Multicores were then slab sampled in 0.5 cm increments and frozen onboard. Once on shore, core tops were freeze-dried and washed through 63 µm sieves. North Pacific sediment samples used for this study were collected via multicore at two stations on cruise AT26-19 of the *RV Atlantis* from 28 August to 11 September 2014 (Fig. 1 and Table 1). The cores were sampled at 1 cm increments and dried core tops were washed using 63 µm sieves. In lieu of North Pacific water column samples, carbonate chemistry was extrapolated from GLODAPv2.2023 (Lauvset et al., 2023; Olsen et al., 2016) (see Sect. 2.2).

https://doi.org/10.5194/egusphere-2026-3333
Preprint. Discussion started: 30 June 2026

| Cruise | Station | Multicore | Lat (°N) | Long (°E) | Water Depth (m) | Sample Depth (cm) | Bottom Water $\Delta[CO_3^{2-}]$ (μmol kg$^{-1}$) | Pore Water $\Delta[CO_3^{2-}]$ (μmol kg$^{-1}$) | *N. pachyderma* Normalized CTDX% (±1σ) | *N. incompta* Normalized CTDX% (±1σ) |
|---|---|---|---|---|---|---|---|---|---|---|
| *Core Top* | | | | | | | | | | |
| CE23011 | 2 | MUCD | 71.63 | -8.42 | 1,898 | 0-0.5 | 30.84 | | 12.34 ± 2.22 | |
| CE23011 | 3 | MUCA | 74.47 | -1.56 | 3,280 | 0-0.5 | 19.42 | | 9.97 ± 1.40<br>8.36 ± 1.54* | |
| CE23011 | 7 | MUCC | 75.83 | -8.18 | 1,971 | 0-0.5 | 35.17 | | 13.66 ± 2.86 | |
| CE23011 | 8.1 | MUCB | 74.25 | -10.07 | 3,088 | 0-0.5 | 11.53 | | 11.85 ± 0.65 | 11.10 ± 1.79 |
| CE23011 | 10 | MUCA | 70.50 | -17.09 | 1,661 | 0-0.5 | 44.73 | | 13.81 ± 1.61 | |
| CE23011 | 19 | MUCA | 57.55 | -48.52 | 3,544 | 0-0.5 | 3.12 | | 11.01 ± 1.25 | |
| CE23011 | 21 | MUCD | 53.54 | -20.29 | 2,172 | 0-0.5 | 32.93 | | | 15.62 ± 3.07 |
| AT26-19 | 06MC | 3 | 44.88 | -130.64 | 2,688 | 0-1 | -12.85 | | | 17.12 ± 4.52 |
| AT26-19 | 53MC | 3 | 44.67 | -130.30 | 2,347 | 0-1 | -10.27 | | 20.28 ± 2.20 | 17.53 ± 3.72 |
| *Downcore* | | | | | | | | | | |
| CE23011 | 2 | MUCD | 71.63 | -8.42 | 1,898 | 1-1.5 | 30.84 | -5.88 [+2.95, -3.42] | 18.04 ± 2.32 | |
| CE23011 | 3 | MUCD | 74.47 | -1.56 | 3,280 | 1.5-2 | 19.42 | -6.24 [+9.83, -5.09] | 10.23 ± 1.22<br>9.27 ± 1.43* | |
| CE23011 | 18 | MUCB | 58.25 | -45.64 | 2,279 | 0.5-1 | 23.93 | 0.49 [+28.45, -10.42] | 10.89 ± 1.01 | 15.85 ± 0.98 |
| CE23012 | 19 | MUCB | 57.55 | -48.52 | 3,544 | 0.5-1 | 3.12 | -11.2 [+19.23, -7.80] | 18.11 ± 1.33 | 22.71 ± 2.65 |
| CE23011 | 22 | MUCC | 53.22 | -18.89 | 2,402 | 0.5-1 | 41.04 | 15.38 [+30.95, -11.75] | | 16.65 ± 1.56 |

*Dextrally coiling *N. pachyderma*

**Table 1—Station data. Pore water $\Delta[CO_3^{2-}]$ is interpolated to the sample depth with the interpolation errors in brackets.**

## 2.2 Carbonate chemistry

North Atlantic and Nordic Sea water column and pore water alkalinity were measured on board cruise CE23011 using an Apollo SciTech Model AS-ALK3 Total Alkalinity Titrator. In short, the titrator uses the principle of Gran titration, adding increments of ~0.1 M HCl to 20 mL aliquots of each sample at 20° C to generate a Gran function and derive total alkalinity. The Orion 8302BNUMD Ross Ultra pH/ATC Triode pH probe was calibrated prior to each day of runs using Thermo Scientific buffers with pH 4.01, 7, and 10.01. The pH of the HCl for titration was then calibrated by titrating Batch 208 of Reference material for Oceanic $CO_2$ measurements prepared by Dr. Andrew Dickson at Scripps Institution of Oceanography a minimum of three times until the relative standard deviation (RSD) of HCl pH calculated from two or more titrations was <0.01 %. Batch 208 was run as a QC standard bracketing every ~5 samples and had a standard deviation of 7.69 μmol kg$^{-1}$ prior to drift correction. Every second CTD sample was analyzed in replicate with an average difference between replicates of 8.43 μmol kg$^{-1}$. Following analysis, alkalinities were converted from μmol L$^{-1}$ to μmol kg$^{-1}$ using the equation of state then drift corrected using Batch 208. Given that the small volumes of pore waters did not allow for aliquots to be saved for DIC analysis, pore water pH was measured prior to titration using the Orion 8302BNUMD Ross Ultra pH/ATC Triode pH probe. Additionally, small pore water sample sizes meant that only two rinses of the titrator rather than three were performed prior to titration and that pore water samples could not be run in replicate. We estimate porewater pH error to be similar to the CTD average replicate difference of 0.017.

DIC for North Atlantic and Nordic Sea CTD samples was measured at the Marine Institute *Foras na Mara* using an LI-5350A DIC analyzer with an LI-850 gas analyzer. The DIC analyzer acidifies 1.5 mL sample aliquots to release all DIC as $CO_2$ gas, which is then measured using the gas analyzer. Batch 208 was run in triplicate aliquots of 1.2 mL, 1.5 mL, and 1.8 mL at the beginning and end of each batch of eight sample triplicates to calibrate the DIC analyzer. Additionally, Batch 208 was analyzed as a QC standard after each batch of eight sample triplicates and triplicate means across all runs had a standard deviation of 1.35 μmol kg$^{-1}$.

North Pacific alkalinity, DIC, salinity, and temperature were taken as the average of the six nearest GLODAPv2.2023 stations (Lauvset et al., 2023; Olsen et al., 2016) to the AT26-19 stations (Figs. 1 and A1). In situ North Atlantic, Nordic Sea, and North Pacific carbonate system chemistry including $\Delta[CO_3^{2-}]$ was calculated from alkalinity and DIC using CO2SYS version 25b06 (Table 1) (Lewis and Wallace, 1998). For all calculations we used constants from Lueker et al. (2000), the Dickson (1990) KSO4, total boron from Uppstrom (1974), KF from Dickson and Riley (1979), and default total phosphate and total silicate. Following similar methods, in situ multicore pore water $\Delta[CO_3^{2-}]$ were calculated using CO2SYS from alkalinity and pH data assuming bottom water pressure, temperature, and salinity. CTD $\Delta[CO_3^{2-}]$ error is propagated from the standard deviation of batch 208 alkalinity and average standard deviation of DIC triplicates. Pacific bottom water $\Delta[CO_3^{2-}]$ errors are the range of the six nearest GLODAP stations. Pore water errors are propagated from the standard deviation of batch 208 alkalinity and the average difference in pH between CTD replicates.

Pore water $\Delta[CO_3^{2-}]$ for unsampled sediment depths were linearly interpolated between the two nearest bracketing pore water samples or between CTD bottom water and the shallowest pore water sample for depths where sediment samples were collected from above the shallowest pore water sample. Error for interpolated pore water $\Delta[CO_3^{2-}]$ is calculated from maximum and minimum possible values in the interpolation window when considering errors for the interpolation endpoints.

### 2.3 µCT scanning and image processing

Eight *N. pachyderma* and eight *N. incompta* tests from the 200-250 µm size fraction were picked from each core top and downcore for µCT scanning. Dextrally coiling specimens with *N. incompta* morphology are present at CE23011 Station 3 at <3-4%, so we classify them as dextrally coiling *N. pachyderma* (e.g., Darling et al., 2006; El Bani Altuna et al., 2018). Core top samples were collected from 0-0.5 cm sediment depth for North Atlantic and Nordic Sea cores and 0-1 cm from Pacific cores (Table 1). Downcore specimens were collected from 0.5 cm sampling increments between 0.5 and 2 cm sediment depth (see Table 1 for specific depths sampled for each core). We scanned 8 specimens per sample as this number is representative of a population (e.g. Iwasaki et al., 2022) along with a crystal of NBS 19 (211-436 µm maximum diameter) as a density standard. Specimens and the standard were attached to a tube made of Kapton in a 3x3 matrix using a thin layer of glue composed of a mixture of tragacanth gum powder and MiliQ water (modified protocol from Coletti et al., 2018). µCT scans were performed at the University of Galway in 1,601 projections at a magnification of 20x using a Zeiss Xradia VERSA 620 with a voltage of 120 kV, a power of 17.50 W, exposure time of 6 s, binning of 1, and no filter. A detector distance of 16.1 mm, source distance of -40.1 mm resulted in a pixel size of 0.49 µm. TXRM images were reconstructed into TXMs using Adaptive Motion Compensation and an Autocentre Shift in the Zeiss Scout and Scan Data Explorer and Reconstructor. An intensity histogram was generated for a line across the background of the first slice of each reconstructed TXM to calculate the average and standard deviation intensities of the background.

TXMs were segmented to isolate the NBS19 crystal and individual *N. pachyderma* and *N. incompta* shells using the cropping function in the program Amira 3D Pro. To segment the NBS19 crystal from each scan, we selected the “masking tool” on “all slices” mode to assign as background all pixels with intensities equal to or less than the average background intensity plus two standard deviations. We then used the “wand tool” on “all slices” mode

https://doi.org/10.5194/egusphere-2026-3333
Preprint. Discussion started: 30 June 2026

to select standard material with intensities ranging between the maximum image intensity and the minimum possible intensity that does not select any non-standard material. This is a more complex thresholding tool that only selects pixels continuously connected via neighboring pixels that meet the threshold to an initial user selected pixel.

Following thresholding steps on the NBS19 crystal, the "watershedding" tool was used to automatically assign the remaining pixels to the standard or background based on the pixels already assigned by the user. This "watershedding" method is appropriate for NBS19 crystals because their regular shape and strong density contrast relative to the background and glue allows for quick and objective segmentation of the crystal. However, minimal density differences between dissolved shell and trapped sediment precludes the use of this method on foraminifera (see Section 4.1).

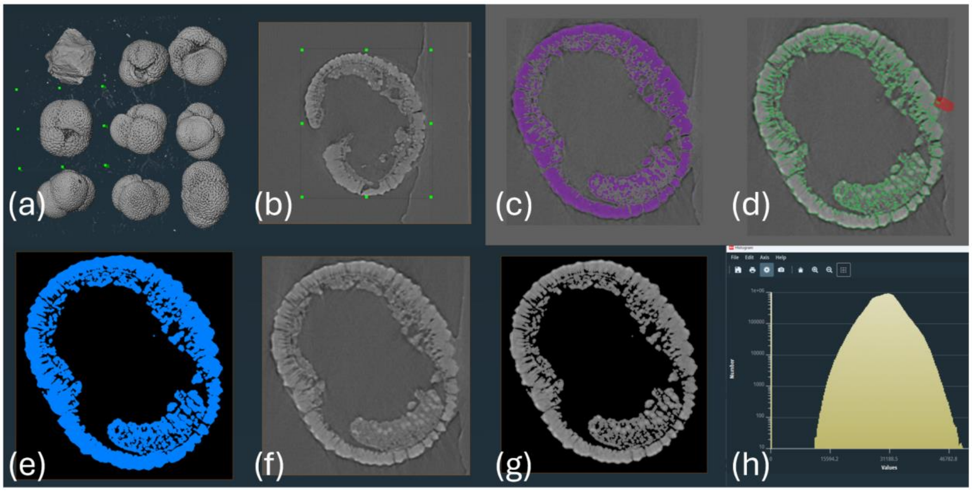

**Figure 2—Thresholding method of processing µCT scans of foraminifera in Amira. (a) the scan is cropped in 3D and then in 2D (b) to include only the specimen of interest. (c) the specimen is then thresholded in the segmentation tab using the wand on all slices mode to remove all material with intensity lower than 73% of the range between the average background intensity and the average intensity of the standard from the same scan. (d) non-test material external to the shell is removed using the paintbrush tool. The selected material is expanded by two pixels, then the segmented image (e) is multiplied by the initial unsegmented image (f) to eliminate all background and material removed via thresholding and using the paintbrush to produce a final processed image (g). An intensity histogram is then generated from the final processed image (h).**

To address this shortcoming, we primarily rely on thresholding when segmenting foraminifera. Briefly, our thresholding method begins with the "wand tool" on "all slices" mode to select the foraminifera test. We used the maximum intensity of the scan as the maximum threshold and calculated the minimum threshold using Eq. (1):

$$\text{Minimum Thresholding Intensity} = \mu_{\text{background}} + 0.73 \text{ x } (\mu_{\text{standard}} - \mu_{\text{background}}) \qquad (1)$$

where $\mu_{\text{background}}$ is the average intensity of the background and $\mu_{\text{standard}}$ is the average intensity of the standard. The Minimum Threshold Intensity was visually identified in several scans to approximately correspond to the

https://doi.org/10.5194/egusphere-2026-3333
Preprint. Discussion started: 30 June 2026

minimum intensity of foraminifera test and the maximum intensity of the tragacanth gum glue, allowing for the selection of primarily foraminiferal test and minimal glue. The "paintbrush tool" was then used to draw over and manually remove any non-test material exterior to the shell wall (primarily tragacanth gum). While this manual removal does introduce minor subjectivity, dissolution is focused on the interior shell walls (e.g., Sect. 4.2.), and the more regular shape of the less dissolved external edges makes differentiating between exterior shell walls and gum relatively easy. Once this step was completed, material labelled as test was expanded by two pixels (~1 μm) to capture test pixels on the edges of the foraminifera, a process also used in Iwasaki et al. (2023).

Following segmentation, NBS19 crystals and foraminifera material in segmented images were assigned a value of 1 and all other materials are assigned a value of 0. Segmented images were then multiplied by the original TXM image to remove all material not identified as NBS19 or shell from the original image. Finally, an intensity histogram was generated from the product image (Fig. 2). We then assign normalized intensity values of 40 and 60 to the average background intensity and standard intensity respectively and calculate normalized intensity from raw intensity. Normalized intensity values less than 0 and greater than 100 are then excluded when calculating our dissolution index. A single scan of 8 NBS19 crystals shows a relative standard deviation between crystal intensities of 1.1 %, while long term comparison of scans using the same crystal shows there is no systematic density drift (Figs. S2 and S3). By normalizing intensity to the average background (air) and standard intensities, our new method allows for direct comparison of normalized intensities across scans and future studies by accounting for differences in voltage and power between scans and scanners.

Values of 40 and 60 were chosen as anchor points for normalization because they place peak normalized pixel counts at a normalized intensity of ~ 60 (Fig. 4), slightly above the typical threshold assigned to low density calcite (Iwasaki et al., 2023) and therefore maximizing variability in our dissolution index (see EQ. 2 and accompanying paragraph). Furthermore, we do not normalize the intensity of air to 0 because we find that a substantial amount of shell material has lower raw intensity than average air, likely because of beam hardening, and would be removed if we did so (Ay et al., 2013; Briguglio et al., 2014). Lastly, these thresholds with air having a normalized intensity above 0 result in <0.5 % of shell pixels, a volume insignificant to the final dissolution index, being removed from by excluding values less than 0 and greater than 100.

We call our new dissolution proxy "normalized CTDX%" (nCTDX% hereafter) and calculate it for each specimen from our normalized intensity curves using Eq. (2):

$$\mathrm{nCTDX\%} = 100 \times (n_{\mathrm{low}} / n_{\mathrm{total}}) \tag{2}$$

where $n_{\mathrm{low}}$ is the normalized number of pixels with a normalized intensity ≤50 and $n_{\mathrm{total}}$ is the total number of pixels in the specimen.

### 2.4 SEM

SEM images were generated at the University of Galway using a Hitachi S-4700 SEM at 10-15 kV and 250-1600x magnification. Prior to imaging, specimens were coated in gold. Specimens were first imaged intact, then gently cracked open to allow for images of internal test walls.

## 3. Results

### 3.1 Bottom water and pore water Δ[$CO_3^{2-}$]

Bottom water Δ[$CO_3^{2-}$] measured from CTD Niskin bottles was above 0 µmol $kg^{-1}$ at all subpolar North Atlantic and Nordic Sea CE23011 stations included in this study, ranging from 3.12 to 44.73 µmol $kg^{-1}$ (Fig. 1 and Table 1). Deepwater Δ[$CO_3^{2-}$] extracted from the GLODAP dataset provide negative Δ[$CO_3^{2-}$] values of -12.85 µmol $kg^{-1}$ for Station 06MC and -10.27 µmol $kg^{-1}$ for Station 53MC (Fig. S1 and Table 1). Pore water Δ[$CO_3^{2-}$] collected from the top 5 cm of multicores range from -17.99 to 43.23 µmol $kg^{-1}$ (Fig. 3). All Stations but 7 and 21 reach negative values within the top 3 cm of the sediment column, with many being undersaturated with respect to carbonate ion by 1 cm.

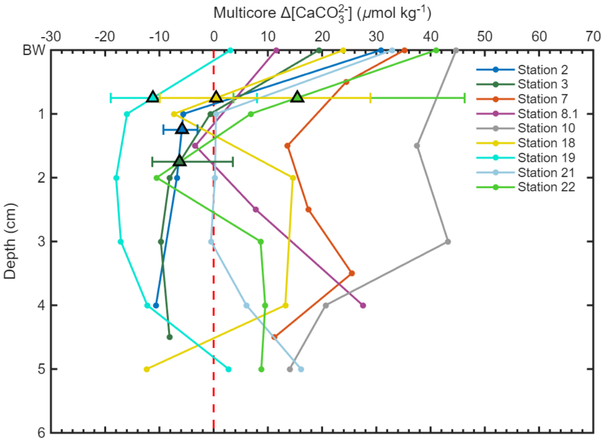

**Figure 3—CE23011 CTD bottom water (BW) and multicore porewater Δ[$CO_3^{2-}$]. Triangles indicate downcore sample depths for *N. pachyderma* and *N. incompta* and interpolated Δ[$CO_3^{2-}$] and error for that depth.**

### 3.2 Δ[$CO_3^{2-}$], normalized intensity profiles, and nCTDX%

*N. pachyderma* and *N. incompta* cross-section density maps and normalized intensity profiles used to calculate nCTDX% are shown in Figs. S4, S5, S6, and S7, and Fig. 4 respectively. There is a clear pattern of high nCTDX% values measured in *N. pachyderma* corresponding to low in situ Δ[$CO_3^{2-}$] (Fig. 5 and Table 1). The same relationship between nCTDX% and in situ Δ[$CO_3^{2-}$] is also valid for *N. incompta* specimens (within uncertainties) from all Stations but 21 and 22, where specimens have high nCTDX% values despite high in situ Δ[$CO_3^{2-}$]. In addition, we note that *N. incompta* nCTDX% for Station 18 are significantly higher than *N. pachyderma* nCTDX% from the same sample.

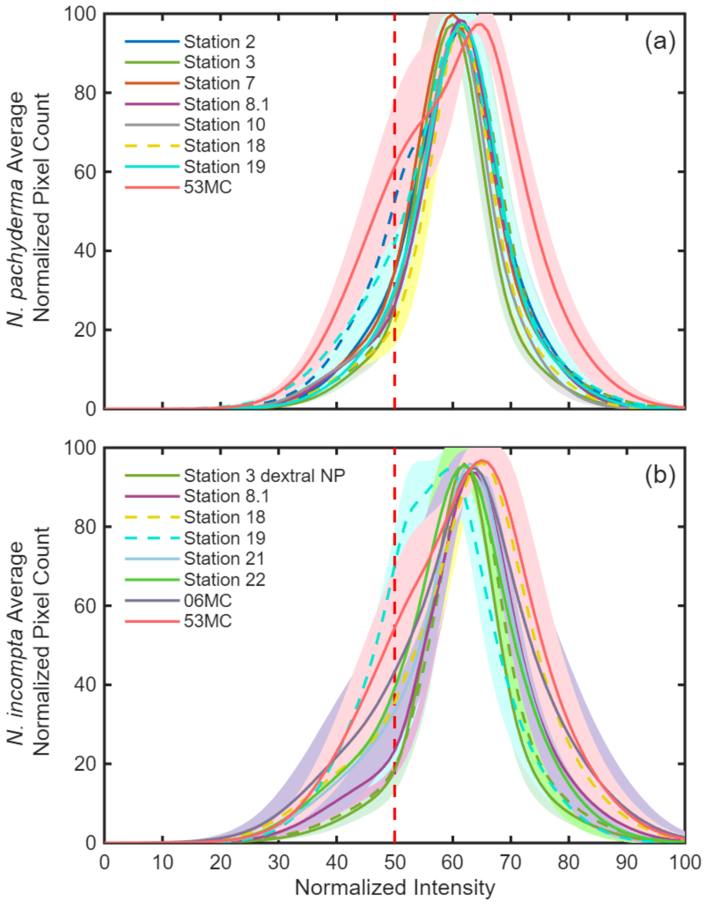

**Figure 4—Normalized pixel counts at each normalized µCT scan intensity averaged for eight *N. pachyderma* (a) and *N. incompta* (b) specimens scanned at each station. Dashed lines indicate downcore samples. Curves of individual specimens were linearly interpolated to intensity intervals of one prior to averaging. Shading represents the standard deviation of each average. nCTDX% are calculated as the percentage of pixels below a normalized intensity of 50 (vertical red dashed line).**

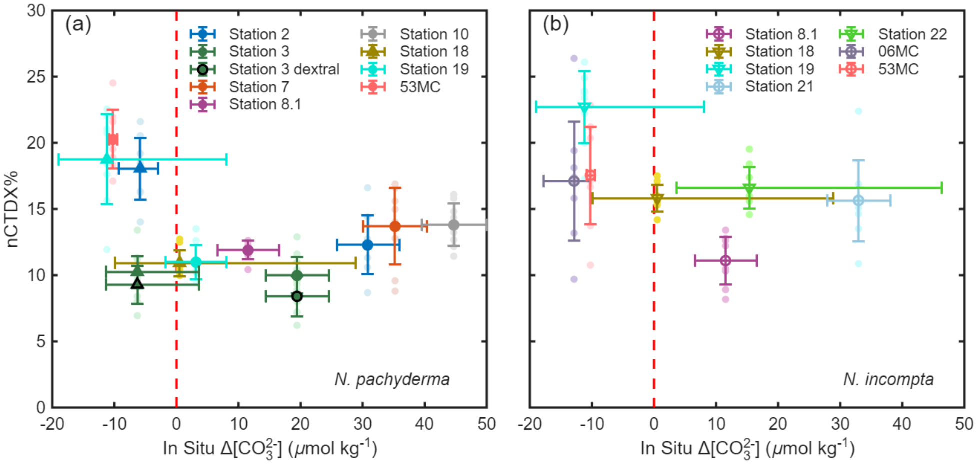

**Figure 5—Core top (large dots and open circles) and downcore (triangles; see Table 1 for sediment depth) nCTDX% vs. in situ Δ[CO$_3^{2-}$] for *N. pachyderma* (a) and *N. incompta* (b). Light-colored small dots represent individual specimens and dark-colored symbols station averages and standard deviations.**

## 4. Discussion

### 4.1 Evaluation of the nCTDX% method

The largest source of subjectivity and most time-consuming task when processing foraminifera and quantifying dissolution from µCT images is the process of removing trapped sediment from segmented images. This is because there is substantial overlap in density between dissolved shell material and sediment, (Johnstone et al., 2010) (e.g. CTS53MCNP2, CTS2Np6, and CTS7Np2 in Figs. S4 and S5). Some studies chose to remove trapped sediment manually based on visual identification (Iwasaki et al. 2019; 2022; and 2023), while others decided to leave trapped sediment in their segmented images to limit subjectivity (Johnstone et al., 2010). Most, if not all, *N. pachyderma* and *N. incompta* specimens included in this study contain some trapped sediment or heavily dissolved shell material that could be interpreted as trapped sediment. Ideally, a pre-scan cleaning step involving ultrasonication such as "HyPerCal" described in Zarkogiannis et al. (2020) should be used to remove trapped sediments prior to analysis. Unfortunately, we found that many *N. pachyderma* and *N. incompta* specimens are too fragile to survive ultrasonication and conclude that such cleaning risks biasing results toward less dissolved specimens by destroying the most fragile and dissolved individuals. Alternatively, a method that utilizes "watershedding" as used here to process NBS19 crystals could allow Amira to more objectively remove sediment from images. However, we found it to be extremely time consuming to train Amira for this task. Furthermore, Amira was unable to satisfactorily distinguish between the two materials because of the minimal density difference between trapped sediment and heavily dissolved material.

Instead, we propose to rely on thresholding to segment the inside of specimen shells. By using average background and standard intensity to calculate a minimum threshold intensity that targets the transition between foraminifera and tragacanth gum adhesive for each scan, we maximize objectivity when removing trapped sediment, while limiting its inclusion in the final reconstructed image. However, we note that the resulting minimum intensity threshold equates to a normalized intensity of ~54, which would result in the exclusion of shell material with normalized intensity below that limit. We address this point by expanding the final selection by two pixels (~0.5

https://doi.org/10.5194/egusphere-2026-3333
Preprint. Discussion started: 30 June 2026

µm) at the end of the segmentation process. This ensures that any shell material on the edges of the thresholded images is captured in the final segmented images. Final segmented images illustrate complete shells (e.g. no artificial holes), supporting this approach (Figs. S4 and S5). Additionally, all the peaks of the normalized pixel count profiles (Fig. 4) and most of the individual specimen profiles (except specimens CTS53MCNP8, DCS19NI4, DCS19NI8) have normalized intensities higher than 54 (Figs. S8 and S9). This ensures that any important pixel count variability in the region around a normalized intensity of 50, the cutoff between high- and low-density shell when calculating nCTDX%, is captured. Although it does not necessarily mean lower intensity peaks aren't removed, which could reduce maximum possible nCTDX% and overall variability in the proxy (see also section 4.4).

Furthermore, we caveat that this approach most likely captures a small volume of what is likely trapped sediment in final segmented images. When consulting cross-sectional density maps (Figs. S4 and S5) it is evident however that the volume of trapped sediment is small relative to the total volume of the specimens suggesting that nCTDX% is not skewed by trapped sediment. For example, many specimens with low nCTDX% (e.g., CTS3DNP8, CTS19NP8, DCS3NP5 and CTS8.1NI8) appear to contain trapped low-density sediment, indicating that the volume of trapped sediments is relatively small and does not lead to high nCTDX%. Likewise, many specimens with high nCTDX% (e.g., CTS53MCNP6, CTS53MCNP5, DCS19BNP1, DCS19NI8, DCS53MCNI8) contain little to no material that could be interpreted as trapped sediments. Taken together, these observations support our argument that trapped sediment is unlikely to significantly influence nCTDX% values.

In summary, thresholding effectively removes subjectivity and is a strength of nCTDX%. Critically, we believe it is fundamental to capture this low-density gap filled material in reconstructions to accurately quantify dissolution intensities. This is because partially dissolved inner shell material is indistinguishable from trapped sediment. Ultimately, we believe that the benefits of increased objectivity when differentiating between heavily dissolved shell material and trapped sediments as well as the significant time savings from this method outweigh the potential downsides of including some trapped sediments and excluding some low-density shell in the final reconstructions.

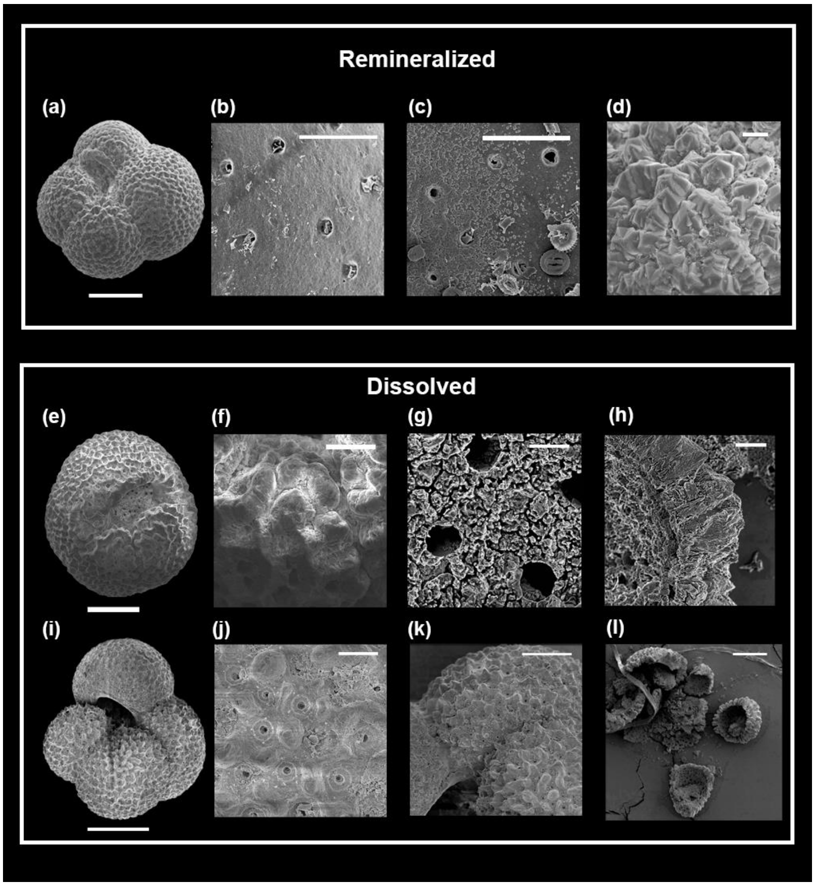

**Figure 6—SEM images of remineralized and partially dissolved specimens. (a-d) core top *N. incompta* specimen CTS21NI5 from carbonate mound Station 21 showing evidence of secondary inorganic calcification. (e-d) core top *N. pachyderma* specimen CTS53MCNP2 from Station 53MC and (i-l) downcore *N. incompta* specimen DCS19NI8 from Station 19 both showing evidence of partial dissolution.**

### 4.2 Dissolution in *N. pachyderma* and *N. incompta*

High core top nCTDX% at stations where bottom water $\Delta[CO_3^{2-}]$ is below 0 µmol kg$^{-1}$ and low nCTDX% for core top specimens where $\Delta[CO_3^{2-}]$ is above 0 µmol kg$^{-1}$ are consistent with previous studies focused on tropical to transitional species (Iwasaki et al., 2015; Iwasaki et al., 2019a; Iwasaki et al., 2019b; Iwasaki et al., 2022; Johnstone et al., 2010; Johnstone et al., 2011; Johnstone et al., 2014) and indicate that carbonate ion saturation controls dissolution in both species (Figs. 5, A4, and A5). Unlike previous studies, however, *N. pachyderma* does not begin to dissolve at bottom water $\Delta[CO_3^{2-}]$ values between 0 and 10 µmol kg$^{-1}$ (e.g., Iwasaki et al. 2023) perhaps indicating that *N. pachyderma* is overall more resistant to dissolution in this range.

https://doi.org/10.5194/egusphere-2026-3333
Preprint. Discussion started: 30 June 2026

Cross-sectional μCT images of specimens from sampling intervals with low bottom water Δ[$CO_3^{2-}$] (e.g., <0 μmol $kg^{-1}$) present clear dissolution patterns. High nCTDX% individuals from these sites (e.g., CTS53MCNP6, CTS53MCNP8, and CTS06MCNI2) have thin external shell walls with internal edges consisting of low-density material (Figs. S4 and S5) that in many cases is patchy and gap-filled, appearing to be heavily dissolved shell material (e.g., CTS53MCNP2, CTS53MCNP3, and CTS06MCNI7). SEM images of an *N. pachyderma* specimen from Station 53MC (e.g., Δ[$CO_3^{2-}$] = - 10.27 μmol $kg^{-1}$) show lattice-like structures incised on the interior surfaces of shell walls (Fig. 6g), that likely represent the patchy gap-filled material seen in μCT images and further demonstrates that dissolution is focused on those interior walls. Dissolution from the inside out is also consistent with evidence from other planktonic foraminifera species (e.g. *Globigerinoides ruber*, *Globigerina bulloides*, *Globoconella inflata*, *Trilobatus sacculifer*, *Neogloboquadrina dutertrei* and *Pulleniatina obliquiloculata*) for which μCT-based dissolution proxies have been developed (Iwasaki et al., 2015; Iwasaki et al., 2019a; Iwasaki et al., 2019b; Iwasaki et al., 2022; Jana et al., 2024.

Many heavily dissolved core top *N. pachyderma* and *N. incompta* specimens (e.g., CTS53MCNP8, CTS53MCNP2, CTS53MCNI4 and CTS53MCNI8) are left with thin outer shell walls, entirely missing internal chambers (Figs. S4 and S5), a phenomenon also observed in other species that form thick gametogenic outer crusts (e.g. *N. dutertrei* and *P. obliquiloculata)* (Johnstone et al., 2010). The resistance of these outer shell walls can be attributed to their low Mg content that characterizes gametogenic crusts in *N. pachyderma*, *N. incompta* (Davis et al., 2017; Hupp and Fehrenbacher, 2023; Jonkers et al., 2016) and other heavily crusted species (Johnstone et al., 2010), which reduces the solubility of calcite (Brown and Elderfield, 1996; Dekens et al., 2002; Rosenthal et al., 2022; Saenger and Evans, 2019; Tierney et al., 2019).

A final feature of dissolution evident in cross-sectional μCT images is the formation of thin elongated low-density features and gaps running parallel to the edges of shell walls (e.g., CTS53MCNP1, CTS53MCNP8, CTS53MCNI3, CTS06MCNI4, and CTS06MCNI7) (Figs. S4 and S5). We attribute these low-density features and gaps to organic laminae (Kunioka et al., 2006) that form between each layer of calcification (Bé, 1980; Fabbrini et al., 2025; Jonkers et al., 2016; Sadekov et al., 2005). These laminae are rich in Mg (Jonkers et al., 2016; Sadekov et al., 2005) and have large crystals (Johnstone et al., 2010), both of which increase shell solubility (Johnstone et al., 2010; Jonkers et al., 2016; Sadekov et al., 2005). These thin laminae (e.g.,< 0.5 um) act as a locus for dissolution, presenting as low-density features (e.g., S06MCNI4) that develop into elongated gaps that create the appearance of double shell walls when dissolution progresses (e.g., S53MCNI3) as suggested in (Johnstone et al. 2010).

In contrast, specimens from stations with positive bottom water Δ[$CO_3^{2-}$] are characterized by thick walls, relatively little low-density features, and well-preserved interior chamber walls in cross-sectional μCT images (Figs. S6 and S7). These features are consistent with previous observations of planktonic foraminifera recovered from bottom water Δ[$CO_3^{2-}$] > 10 μmol $kg^{-1}$ (Iwasaki et al., 2015; Iwasaki et al., 2019a; Iwasaki et al., 2019b; Iwasaki et al., 2022; Jana et al., 2024; Johnstone et al., 2010; Johnstone et al., 2011; Johnstone et al., 2014).

### 4.3 Undersaturated pore water as a driver of dissolution

https://doi.org/10.5194/egusphere-2026-3333
Preprint. Discussion started: 30 June 2026

The sediment depth at which respiration of organic matter leads to undersaturated pore waters in $\Delta[CO_3^{2-}]$ can vary by region and depositional environment (Cetiner et al., 2025; Iwasaki et al., 2023; Martin and Sayles, 1996). However, several investigations estimate that respiration-driven dissolution of carbonates deposited in offshore marine sediments can begin within the top 5 cm of the sediment column (Cetiner et al. 2025, Martin and Sayles 1996). Our combination of downcore nCTDX% and bottom and pore water data provides a unique opportunity to investigate if pore water driven dissolution in the top 2 cm of marine sediments affects nCTDX% values recorded in *N. pachyderma* and *N. incompta* specimens.

Downcore *N. pachyderma* and *N. incompta* specimens were analyzed at four North Atlantic and one Nordic Seas station (Table 1), all with bottom water $\Delta[CO_3^{2-}] > 0$ µmol kg$^{-1}$. Meanwhile, core top specimens from these stations have low nCTDX% values and show no dissolution features in cross-sectional images, indicating modern bottom water is not driving dissolution at these stations. In contrast, downcore specimens from Stations 2 and 19 have high nCTDX% (Fig. 5) and appear heavily dissolved in cross sectional µCT (Figs. S6 and S7) and SEM images (Figs. 6a to 6d). Porewater $\Delta[CO_3^{2-}]$ for these specimens are $< 0$ µmol kg$^{-1}$, strongly suggesting that porewater chemistry could be driving dissolution in shallow marine sediments. Alternatively, undersaturated bottom water $\Delta[CO_3^{2-}]$ (Fig. 3) at the time of deposition could have led to the partial dissolution of these specimens. However, the young age of sediments from nearby cores (Davies et al., 2021; Jung, 2004; Nørgaard-Pedersen et al. 2003) (e.g., <5 ka, supplementary Table S1), and previous estimates that indicate North Atlantic bottom water $\Delta[CO_3^{2-}]$ decreased by less than 4 µmol kg$^{-1}$ over the last 5 ka (Broecker et al., 1999; Zeebe., 2012) suggest that this scenario is unlikely.

In contrast to Stations 2 and 19, downcore specimens from Station 3 have low nCTDX% (Figs. 3 and 4) and cross sectional µCT images illustrate thick intact shell walls for sinistral and dextral coiling *N. pachyderma* specimens (Figs. S6 and S7) despite low interpolated $\Delta[CO_3^{2-}]$ values ranging between 3.59 and -11.33 µmol kg$^{-1}$. A possible explanation could be that the linearly interpolated $\Delta[CO_3^{2-}]$ values are misrepresenting actual porewater gradients, which do not always decrease gradually over the water sediment interface. Instead, microsensor profiling studies have shown that abrupt transitions in $[CO_3^{2-}]$ are possible within millimeters (Han et al., 2014; Rassmann et al., 2016). It is thus entirely possible that the transition between saturated to undersaturated porewaters occurred below the sampling depth at Station 3 of 1.5-2 cm and low nCTDX% values measured in *N. pachyderma* adequately represent the saturation state from this interval.

As at Station 3, porewater $\Delta[CO_3^{2-}]$ values for specimens analyzed at Station 18 straddle undersaturated and saturated conditions (-9.93 to 28.94 µmol kg$^{-1}$). Interestingly, *N. pachyderma* exhibits significantly lower nCTDX% values than *N. incompta* at this Station 18. Considering that *N. incompta* has consistently higher Mg content than *N. pachyderma* (Nyland et al., 2006), the higher nCTDX% may illustrate the fact that *N. incompta* is slightly more susceptible to dissolution than *N. pachyderma* when bathed in porewaters that approach values ~ 0 µmol kg$^{-1}$ (Brown and Elderfield, 1996). We conclude that pore waters undersaturated in carbonate ion will initiate partial dissolution of *N. pachyderma* and *N. incompta* specimens in sediments as shallow as 0.5-1 cm from the water – sediment interface and that this signal is captured by the nCTDX% proxy.

### 4.4 nCTDX% as an indicator of secondary inorganic precipitation

https://doi.org/10.5194/egusphere-2026-3333
Preprint. Discussion started: 30 June 2026

Stations 21 and 22 were collected from the Rockall Bank, a carbonate mound characterized by carbonate sediments and carbonate platforms (limestones, skeletal debris, and biogenic carbonates (Van der Land et al., 2010). Here we analyzed *N. incompta* specimens from the core top of Station 21 and downcore of Station 22. For both samples, nCTDX% values are elevated and thus suggestive of dissolution. However, cross-sectional µCT images display thick inner and outer shell walls characteristic of undissolved specimens (Figs. S6 and S7). Further investigation using SEM images revealed abnormal rhombohedral crystallography on natural topographic highs of the external shell wall (Fig. 6d) that is similar in morphology to high- Mg overgrowth reported by Morley et al. (2017) at nearby Station MC48 (54.7° N, 18.7° W) and at other carbonate banks (Boussetta et al., 2011; Hoogakker et al., 2009; Reuning et al., 2005; van Raden et al., 2011).

Secondary overgrowths can be difficult to detect. This is because secondary precipitation replaces existing topographical highs, making it impossible to differentiate from original shell structures using optical microscopy (Boussetta et al., 2011; Morley et al., 2017; Hoogakker et al., 2009; Reuning et al., 2005; van Raden et al., 2011) or cross-sectional µCT images (Figs. S5 and S7). In addition, supersaturated $\Delta[CO_3^{2-}]$ are not a sole determinant for carbonate minerals to precipitate because kinetic barriers and lack of nucleation sites can prevent mineral formation (James et al., 2021, Turchyn et al., 2021). However, precipitation is more likely to occur near or on existing carbonate structures, such as carbonate mounds, because these provide nucleation surfaces that lower kinetic barriers and stabilize crystal growth. In these microenvironments, local saturation and surface availability combine to promote inorganic carbonate formation (Van der Land et al., 2010).

Biogenic $CaCO_3$ crystals, as found in foraminiferal shells, are often encased in organic matrices and exhibit complex ultrastructures, resulting in higher specific surface area and internal porosity compared with abiotic carbonates (Procter et al., 2024). During early diagenesis, inorganic carbonate overgrowths precipitate on foraminifera shells as smaller, poorly ordered crystals with higher micro- and nano-porosity, which can manifest as lower bulk density in µCT imaging compared with the original biogenic shell. These contrasts in microstructure and composition have been documented in experimental comparisons of biogenic and inorganic carbonates (e.g., Roza-Llera et al., 2024) and in observations of diagenetic inorganic overgrowths on foraminiferal shells in marine sediments (Edgar et al., 2015). Therefore, the appearance of less dense inorganic carbonate crystals on foraminiferal surfaces is consistent with known microstructural and compositional differences between biogenic and secondary carbonate phases, reflecting both porosity and crystal packing differences.

We conclude that the high nCTDX% values for specimens from Stations 21 and 22 are the result of secondary overgrowth. Furthermore, we argue that nCTDX% can be used as a new tool for detecting diagenetic overgrowth and that it can be applied to both core top and downcore samples where diagenetic overgrowth may be difficult to detect otherwise. This recommendation has implications for the application and interpretation of µCT-based proxies discussed in the next section.

## 4.5 nCTDX% as an indicator of Diagenesis

In the previous sections of the discussion, we have shown that high nCTDX% values can detect dissolution linked to undersaturated bottom waters, and undersaturated porewaters, even where bottom waters are supersaturated with respect to calcite. The consistency of the relationship between nCTDX% and in situ $\Delta[CO_3^{2-}]$ across depositional environments suggests that time dissolving is not a dominant factor in dissolution intensity. In addition, we have shown that high nCTDX% can be indicative of early diagenetic overgrowth on the outside of planktonic foraminifera shells. These findings suggest that high nCTDX% values measured in planktonic foraminifera are an indicator for both types of diageneses rather than dissolution alone, and we suggest an nCTDX% threshold value of 15, as an indicator for the diagenetic alteration of specimen (Fig. 7). To differentiate between dissolution and diagenetic overgrowth, we recommend that elevated nCTDX% values are always evaluated in conjunction with cross-sectional density maps of specimens to evaluate the preservation state of internal test walls. If internal test walls are intact despite high nCTDX% values, diagenetic overgrowth should be considered when interpreting geochemical proxies. Furthermore, we advocate for use of supporting proxies (e.g., Br/Ca, planktonic $\delta^{13}C$, and planktonic-benthic $\delta^{13}C$ gradients) that may inform on changes in porewater rather than bottom water saturation state (e.g., Iwasaki et al 2022, Johnstone et al. 2010).

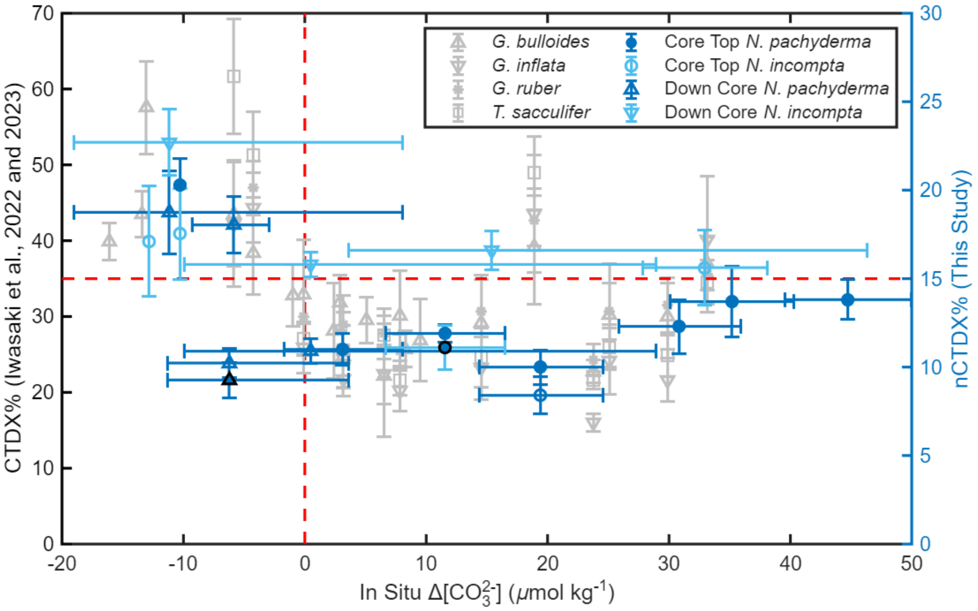

**Figure 7—Scaled comparison between nCTDX% and CTDX% plotted against in situ $\Delta[CO_3^{2-}]$. Core top (dots and open circles) and downcore (triangles) *N. pachyderma* and *N. incompta* nCTDX% from this study are plotted in blue and CTDX% from Iwasaki et al. (2022 and 2023) in gray. Dextral *N. pachyderma* from this study have black outlines. Vertical error bars for both studies are 95% confidence intervals. Horizontal error bars for this study are calculated as in Fig. 3.**

When comparing our results to other planktonic foraminifera species, nCTDX% values compare well with CTDX% values reported in Iwasaki et al. (2022) and Iwasaki et al. (2023), when scaled to account for the different processing methods (Fig. 7). The similarity between species indicates that the relationship between in situ $\Delta[CO_3^{2-}]$ and dissolution as represented by µCT scans is strong and that the methods are properly capturing dissolution dynamics, unless diagenetic overgrowth occurs. The suggested threshold of 15 in nCTDX% values scales to a CTDX% of ~35 based on the consistent relationship between scaled nCTDX% and CTDX% and in situ $\Delta[CO_3^{2-}]$. This threshold not only captures dissolved *G. bulloides, G. ruber* and *T. sacculifer* specimens due to low bottom water $\Delta[CO_3^{2-}]$ but also dissolution at sites where low porewater $\Delta[CO_3^{2-}]$ is suspected to be responsible for dissolution (Iwasaki et al. 2023).

When unscaled, the absolute values and variability in nCTDX% values for *N. pachyderma* and *N. incompta* are lower than the variability in CTDX% values derived for the four tropical species analyzed in (Iwasaki et al 2023) (Fig. 7). We primarily attribute lower nCTDX% values and variability to the difference in segmentation methods. As explained in Section 4.1, objective thresholding necessarily excludes some low-density shell material which is captured by the CTDX% method (manual segmentation). As a result, thresholding may prevent the formation of secondary intensity peaks as seen by Iwasaki et al. (2022; 2023) and Jana et al. (2024). Alternatively, increased resistance to dissolution of *N. pachyderma* and *N. incompta* due to their lower bulk Mg concentrations and thick gametogenic crusts (Brown and Elderfield, 1996; Hemleben et al., 1989; Kucera, 2007) may also contribute to their low nCTDX% values variability.

### 4.6 Implications for paleoclimate reconstructions

Our results confirm that partial dissolution of *N. pachyderma* and *N. incompta* preferentially dissolves internal shell structures (e.g. ontogenetic calcite and laminae) that have previously been shown to be enriched in Mg and have low $\delta^{18}O$ values relative to full shell averages (Bauch et al., 1997; Davis et al., 2017; Hupp and Fehrenbacher, 2023; Jonkers et al., 2016; Kozdon et al., 2009; Westgård et al., 2026). By inference, partial dissolution would leave behind gametogenic crusts that are depleted in Mg and have high $\delta^{18}O$ relative to undissolved bulk shell values (Bauch et al., 1997; Kozdon et al., 2009; Kunioka et al., 2006). As suggested previously, these findings caution that partial dissolution may bias paleoclimate reconstructions (e.g., Dekens et al., 2002; Iwasaki et al., 2023; Johnstone et al., 2010; Rosenthal et al., 2022; Saenger and Evans, 2019; Tierney et al., 2019). However, here we highlight that the impact of partial dissolution on whole shell chemistry varies significantly between species. For example the intratest $\delta^{18}O$ difference between inner (ontogenetic) and outer crust (gametogenic) calcite is relatively small for *G. bulloides* at ~0.6 ‰ (Spero and Lea, 1996), which results in an even smaller difference of <0.2 ‰ between crust calcite and the whole shell of the pristine undissolved specimen because the outer calcite comprises the majority of the total shell (Jana et al., 2024). Such minimal difference in $\delta^{18}O$ values between shell features limits the potential amplitude of a partial dissolution signal that Jana et al. (2024) show is obscured by variability in seasonality, calcification depth, and calcification intensity among other variables.

In contrast, the difference between ontogenetic and gametogenic calcite in *N. pachyderma* is much larger, with gametogenic calcite $\delta^{18}O$ values enriched in $O^{18}$ by as much as ~2 ‰ (Hupp and Fehrenbacher, 2023; Kozdon et al., 2009; Morley et al., 2024). Considering that gametogenic calcite accounts for 40-70% of the final volume of *N. pachyderma* (Hupp and Fehrenbacher, 2023), the impact of partial dissolution of ontogenetic calcite is likely far greater than for *G. bulloides*. For example, assuming a 50:50 contribution between ontogenetic and gametogenic calcite, and the total dissolution of the former, we would expect whole test $\delta^{18}O$ to increase by ~1 ‰ corresponding to a decrease of 4.0-4.5 C in reconstructed temperatures (Kim and O'Neil, 1997) when compared to undissolved specimens. Even the partial dissolution of the internal test walls could potentially bias reconstructed temperatures by 1-2° C.

Similarly, intratest variability of Mg/Ca in *N. pachyderma* suggests gametogenic calcite is lower than ontogenetic calcite (Hupp and Fehrenbacher, 2023; Westgård et al., 2026) with an estimated whole test difference of 15 % (Jonkers et al., 2016). Following the Mg/Ca calibration equation from Morley et al. (2024) and assuming again a 50:50 contribution between ontogenetic and gametogenic calcite, and the total dissolution of the former we would expect ~0.7° C lower SST reconstructions. As for $\delta^{18}$O values the dissolution effect would be lessened if internal test walls were only partially dissolved.

The impact of diagenetic overgrowth on the geochemical composition of *N. pachyderma and N. incompta* specimens is equally important to consider. Morley et al. (2017) linked abnormal rhombohedral crystals on *N. incompta* specimens with elevated Mg/Ca values, noting a departure of 36.5% from the theoretical Mg/Ca-temperature calibration equation which is the equivalent to +2-3° C based on the Morley et al. (2017) calibration. Even larger departures from expected Mg/Ca temperature relationships were observed in Jong et al. (2026) for *N. pachyderma* specimens recovered from Arctic downcore sediments. Using quantitative Energy Dispersive X-ray Spectroscopy (EDS) mapping and SEM images, they explained high Mg overgrowth on the outside of shells to high Mg/Ca values.

We summarize that our findings are important for two reasons. First, the potential influence of shallow porewater dissolution on geochemical proxies is often ignored for the Quaternary and certainly for the current Holocene (e.g., Sejrup et al., 2011; Moffa-Sánchez et al., 2014). Our results suggest that this approach needs to be reevaluated urgently, especially for depositional settings that are likely to experience undersaturated pore waters such as the high accumulating drift sediments of the subpolar North Atlantic. These settings are unique for reconstructing past multidecadal climate variability, bridging the gap between instrumental and paleo timescales. Reevaluating whether partial dissolution impacts shell geochemistry in these settings is thus essential especially when testing climate critical hypothesis (e.g., the warming hole hypothesis Rahmstorf et al. 2015).

Furthermore, when the potential impact of dissolution is considered as a mechanism, often in reconstructions of deeper time climates of the Miocene and beyond, many studies and or Mg/Ca calibrations only consider reconstructions of bottom water and not pore water carbonate ion concentrations as a means to dismiss dissolution (e.g., Kubota et al., 2019) or correct calibrations (e.g., Dekens et al., 2002; Rosenthal et al., 2022; Saenger and Evans, 2019; Tierney et al., 2019). Our results show that reconstructions of bottom water carbonate ion concentrations (e.g. B/Ca on epibenthic foraminifera) cannot rule out the possibility of partial dissolution. This leads us to our second important finding: µCT-based proxies are not suitable to reconstruct past bottom water $\Delta[CO_3^{2-}]$ (Iwasaki et al 2023). Our results suggest the same is true for other dissolution-based proxies such as shell fragmentation and size normalized shell weight. Instead, µCT-based proxies the potential for much more diverse applications in paleoceanographic research acting as a compass guiding the interpretation of geochemical signals recorded in planktonic foraminifera from the recent and distant past.

## 5. Conclusion

Our new method for segmenting foraminifera µCT scans and calculating nCTDX% combines speed and objectivity. By thresholding images using background and standard intensity, we eliminate the need to distinguish between trapped sediments and heavily dissolved shell material, while maintaining normalization to an NBS 19 crystal as a density standard. Our results confirm that like other tropical to transitional species (Iwasaki et al., 2023; Johnstone et al., 2010), *N. pachyderma* and *N. incompta* dissolve from the inside out, leaving behind thin crusts without inner shell walls.

When applied to core tops, nCTDX% correctly identifies undersaturated bottom waters (e.g., $\Delta[CO_3^{2-}] < 0$ µmol kg$^{-1}$). We also demonstrate that undersaturated porewaters within the top 2 cm of the water sediment interface can lead to dissolution even if bottom waters are saturated, suggesting that µCT and other dissolution-basedproxies are a measure of in situ $\Delta[CO_3^{2-}]$ rather than bottom water $\Delta[CO_3^{2-}]$. This finding also highlights that marine archives from the North Atlantic and Nordic Seas are not immune to the impact of dissolution, as is often assumed in paleoceanographic reconstructions. Consequently, we encourage further investigations into the paleoceanographic impact on geochemical proxies that may result from undersaturated porewaters, highlighting particularly vulnerable settings such as fast-accumulating drift deposits in the subpolar North Atlantic, where rapid sedimentation could result in greater deposition and remineralization of organic matter.

Furthermore, our results show that nCTDX% can detect secondary inorganic overgrowth and as a result can be applied downcore not only to investigate dissolution but also diagenetic overgrowth, which may be particularly useful when investigating deep-time archives where this type of diagenesis is an important consideration for interpreting shell geochemistry (e.g., Groeneveld et al., 2008).

## Code and data availability

Data are shared with reviewers via a Zenodo link to a private data set and will be made publicly available in a FAIR repository upon publication.

## Author contribution

T.W. developed and applied the new microCT and image processing methods, analyzed alkalinity and DIC from water column and pore water samples, carried out data analysis and visualization, and wrote the original draft of the manuscript. A.M. was the Chief Scientist on CE23011, conceptualized the project, acquired funding, supervised T.W., assisted with data analysis, and contributed to the final version of this manuscript. A.F. supported TW with microCT scanning, method development on AMIRA Pro, conducted SEM imaging and generated related figures, and contributed to the final version of this manuscript. E.D.L.V. and H.K. contributed to the analysis of Alkalinity and DIC from water column and pore water samples and contributed to the final version of this manuscript. J.M. was co-Chief Scientist on the AT26-19 cruise and contributed samples from the Pacific to this study and contributed to the final version of this manuscript.

## Competing interests

The contact author has declared that neither they nor their co-authors have any competing interests.

## Acknowledgements

We gratefully acknowledge the support of the crew on the RV Celtic Explorer sailing under Master Anthony Hobin. We gratefully acknowledge Dr. Juan Alberto Panadero Pérez for his support with µCT scanning. Authors gratefully acknowledge the facilities, scientific and technical assistance of Dr. Eadaoin Timmins, Centre for Microscopy and Imaging, University of Galway, Ireland (https://imaging.universityofgalway.ie/imaging/) for SEM images.

## Financial support

A.M. acknowledges funding by Research Ireland and the Geological Survey of Ireland under the SFI Frontiers for the Future Programme 21/FFP-P/10261, iCRAG the Science Foundation Ireland Research Centre for Applied Geosciences, under Grant Number 13/RC/2092_P2, and Grant in Aid funding from the Marine Institute for research expedition CE23011 on the RV Celtic Explorer. The contribution of J.F.M. to this study was supported in part by US-NSF award OCE-24-42513.

## References

Anand, P., Elderfield, H., and Conte, M. H.: Calibration of Mg/Ca thermometry in planktonic foraminifera from a sediment trap time series, Paleoceanography, 18, 2002PA000846, https://doi.org/10.1029/2002PA000846, 2003.

Archer, D. and Maier-Reimer, E.: Effect of deep-sea sedimentary calcite preservation on atmospheric $CO_2$ concentration, Nature, 367, 260–263, https://doi.org/10.1038/367260a0, 1994.

Archer, D., Winguth, A., Lea, D., and Mahowald, N.: What caused the glacial/interglacial atmospheric $pCO_2$ cycles?, Reviews of Geophysics, 38, 159–189, https://doi.org/10.1029/1999RG000066, 2000.

Ay, M. R., Mehranian, A., Maleki, A., Ghadiri, H., Ghafarian, P., and Zaidi, H.: Experimental assessment of the influence of beam hardening filters on image quality and patient dose in volumetric 64-slice X-ray CT scanners, Physica Medica, 29, 249–260, https://doi.org/10.1016/j.ejmp.2012.03.005, 2013.

Bauch, D., Carstens, J., and Wefer, G.: Oxygen isotope composition of living *Neogloboquadrina pachyderma* (sin.) in the Arctic Ocean, Earth and Planetary Science Letters, 146, 47–58, https://doi.org/10.1016/S0012-821X(96)00211-7, 1997.

Bauch, D., Darling, K., Simstich, J., Bauch, H. A., Erlenkeuser, H., and Kroon, D.: Palaeoceanographic implications of genetic variation in living North Atlantic *Neogloboquadrina pachyderma*, Nature, 424, 299–302, https://doi.org/10.1038/nature01778, 2003.

Bé, A. W. H.: Gametogenic calcification in a spinose planktonic foramnifer, *Globigerinoides sacculifer* (Brady), Marine Micropaleontology, 5, 283–310, 1980.

Berger, W. H.: Planktonic Foraminifera: Selective solution and the lysocline, Marine Geology, 8, 111–138, https://doi.org/10.1016/0025-3227(70)90001-0, 1970.

Bertlich, J., Gussone, N., Berndt, J., Arlinghaus, H. F., and Dieckmann, G. S.: Salinity effects on cultured *Neogloboquadrina pachyderma* (sinistral) from high latitudes: new paleoenvironmental insights, Geo-Mar Lett, 41, 2, https://doi.org/10.1007/s00367-020-00677-1, 2021.

Boussetta, S., Bassinot, F., Sabbatini, A., Caillon, N., Nouet, J., Kallel, N., Rebaubier, H., Klinkhammer, G., and Labeyrie, L.: Diagenetic Mg-rich calcite in Mediterranean sediments: Quantification and impact on foraminiferal Mg/Ca thermometry, Marine Geology, 280, 195–204, https://doi.org/10.1016/j.margeo.2010.12.011, 2011.

Boyle, E. A.: Vertical Oceanic Nutrient Fractionation and glacial/interglacial $CO_2$ Cycles, Nature, 331, 55–56, 1988.

Briguglio, A., Wöger, J., Wolfgring, E., and Hohenegger, J.: Changing Investigation Perspectives: Methods and Applications of Computed Tomography on Larger Benthic Foraminifera, in: Approaches to Study Living Foraminifera, edited by: Kitazato, H. and M. Bernhard, J., Springer Japan, Tokyo, 55–70, https://doi.org/10.1007/978-4-431-54388-6_4, 2014.

Broecker, W. and Clark, E.: A dramatic Atlantic dissolution event at the onset of the last glaciation, Geochem Geophys Geosyst, 2, 2001GC000185, https://doi.org/10.1029/2001GC000185, 2001.

Broecker, W. S., Clark, E., McCorkle, D. C., Peng, T., Hajdas, I., and Bonani, G.: Evidence for a reduction in the carbonate ion content of the deep sea during the course of the Holocene, Paleoceanography, 14, 744–752, https://doi.org/10.1029/1999PA900038, 1999.

Brown, S. J. and Elderfield, H.: Variations in Mg/Ca and Sr/Ca ratios of plaktonic foraminifera caused by postdepositional dissolution: Evidence of shallow mg-dependent dissolution, Paleoceanography and Paleoclimatology, 11, 543–551, 1996.

Cetiner, J. E. P., Berelson, W. M., Rollins, N. E., Liu, X., Pavia, F. J., Waldeck, A. R., Dong, S., Fleger, K., Barnhart, H. A., Quinan, M., Wani, R. P., Rafter, P. A., Jacobson, A. D., Byrne, R. H., and Adkins, J. F.: Carbonate dissolution fluxes in deep-sea sediments as determined from in situ porewater profiles in a transect across the saturation horizon, Geochimica et Cosmochimica Acta, 390, 145–159, https://doi.org/10.1016/j.gca.2024.11.027, 2025.

Chanda, P., Gorski, C. A., Oakes, R. L., and Fantle, M. S.: Low temperature stable mineral recrystallization of foraminiferal tests and implications for the fidelity of geochemical proxies, Earth and Planetary Science Letters, 506, 428–440, https://doi.org/10.1016/j.epsl.2018.11.011, 2019.

Coletti, G., Stainbank, S., Fabbrini, A., Spezzaferri, S., Foubert, A., Kroon, D., and Betzler, C.: Biostratigraphy of large benthic foraminifera from Hole U1468A (Maldives): a CT-scan taxonomic approach, Swiss J Geosci, 111, 523–536, https://doi.org/10.1007/s00015-018-0306-7, 2018.

Darling, K. F., Kucera, M., Kroon, D., and Wade, C. M.: A resolution for the coiling direction paradox in *Neogloboquadrina pachyderma*, Paleoceanography, 21, 2005PA001189, https://doi.org/10.1029/2005PA001189, 2006.

Davies, S., Stow, D., and Nicholson, U.: Late glacial to Holocene sedimentary facies of the Eirik Drift, southern Greenland margin: Spatial and temporal variability and paleoceanographic implications, Marine Geology, 440, 106568, https://doi.org/10.1016/j.margeo.2021.106568, 2021.

Davis, C. V., Fehrenbacher, J. S., Hill, T. M., Russell, A. D., and Spero, H. J.: Relationships Between Temperature, pH, and Crusting on Mg/Ca Ratios in Laboratory-Grown *Neogloboquadrina* Foraminifera, Paleoceanography, 32, 1137–1152, https://doi.org/10.1002/2017PA003111, 2017.

De Araújo, O. M. O., Aguilera, O., Machado, A. S., De Oliveira, D. F., Leitão, R. G., Dos Anjos, M. J., and Lopes, R. T.: Analysis of Diagenetic Impacts on Foraminifera by X-Rays Techniques, X-Ray Spectrometry, 54, 773–783, https://doi.org/10.1002/xrs.70012, 2025.

Dekens, P. S., Lea, D. W., Pak, D. K., and Spero, H. J.: Core top calibration of Mg/Ca in tropical foraminifera: Refining paleotemperature estimation, Geochem Geophys Geosyst, 3, 1–29, https://doi.org/10.1029/2001GC000200, 2002.

Dickson, A. G.: Standard potential of the reaction: AgCl(s) + 12H$_2$(g) = Ag(s) + HCl(aq), and and the standard acidity constant of the ion HSO$_4^-$ in synthetic sea water from 273.15 to 318.15 K, The Journal of Chemical Thermodynamics, 22, 113–127, https://doi.org/10.1016/0021-9614(90)90074-Z, 1990.

Dickson, A. G. and Riley, J. P.: The estimation of acid dissociation constants in seawater media from potentionmetric titrations with strong base. I. The ionic product of water — Kw, Marine Chemistry, 7, 89–99, https://doi.org/10.1016/0304-4203(79)90001-X, 1979.

Edgar, K. M., Anagnostou, E., Pearson, P. N., and Foster, G. L.: Assessing the impact of diagenesis on $\delta^{11}$B, $\delta^{13}$C, $\delta^{18}$O, Sr/Ca and B/Ca values in fossil planktic foraminiferal calcite, Geochimica et Cosmochimica Acta, 166, 189–209, https://doi.org/10.1016/j.gca.2015.06.018, 2015.

El Bani Altuna, N., Pieńkowski, A. J., Eynaud, F., and Thiessen, R.: The morphotypes of Neogloboquadrina pachyderma: Isotopic signature and distribution patterns in the Canadian Arctic Archipelago and adjacent regions, Marine Micropaleontology, 142, 13–24, https://doi.org/10.1016/j.marmicro.2018.05.004, 2018.

Emerson, S. and Bender, M.: Carbon fluxes at the sediment-water interface of the deep-sea: calcium carbonate preservation, Journal of Marine Research, 39, 139–162, 1981.

Fabbrini, A., Pearson, P. N., Brombacher, A., Iacoviello, F., Ezard, T. H. G., and Wade, B. S.: Morphology of *Pulleniatina* (planktonic foraminifera) from optical microscopy, micro-CT, and SEM investigations, J. Micropalaeontol., 44, 213–235, https://doi.org/10.5194/jm-44-213-2025, 2025.

Groeneveld, J., Nürnberg, D., Tiedemann, R., Reichart, G., Steph, S., Reuning, L., Crudeli, D., and Mason, P.: Foraminiferal Mg/Ca increase in the Caribbean during the Pliocene: Western Atlantic Warm Pool formation, salinity influence, or diagenetic overprint?, Geochem Geophys Geosyst, 9, 2006GC001564, https://doi.org/10.1029/2006GC001564, 2008.

Han, C., Cai, W.-J., Wang, Y., and Ye, Y.: Calibration and evaluation of a carbonate microsensor for studies of the marine inorganic carbon system, J Oceanogr, 70, 425–433, https://doi.org/10.1007/s10872-014-0243-7, 2014.

Hemleben, C., Spindler, M., and Anderson, O. R.: Modern Planktonic Foraminifera, 1st ed., Springer New York, 363 pp., 1989.

Henehan, M. J., Evans, D., Shankle, M., Burke, J. E., Foster, G. L., Anagnostou, E., Chalk, T. B., Stewart, J. A., Alt, C. H. S., Durrant, J., and Hull, P. M.: Size-dependent response of foraminiferal calcification to seawater carbonate chemistry, Biogeosciences, 14, 3287–3308, https://doi.org/10.5194/bg-14-3287-2017, 2017.

Hoogakker, B. A. A., Klinkhammer, G. P., Elderfield, H., Rohling, E. J., and Hayward, C.: Mg/Ca paleothermometry in high salinity environments, Earth and Planetary Science Letters, 284, 583–589, https://doi.org/10.1016/j.epsl.2009.05.027, 2009.

Hupp, B. N. and Fehrenbacher, J. S.: Geochemical Differences Between Alive, Uncrusted and Dead, Crusted Shells of *Neogloboquadrina pachyderma* : Implications for Paleoreconstruction, Paleoceanog and Paleoclimatol, 38, e2023PA004638, https://doi.org/10.1029/2023PA004638, 2023.

Husum, K. and Hald, M.: Arctic planktic foraminiferal assemblages: Implications for subsurface temperature reconstructions, Marine Micropaleontology, 96–97, 38–47, https://doi.org/10.1016/j.marmicro.2012.07.001, 2012.

Iwasaki, S., Kimoto, K., Sasaki, O., Kano, H., Honda, M. C., and Okazaki, Y.: Observation of the dissolution process of *Globigerina bulloides* tests (planktic foraminifera) by X-ray microcomputed tomography, Paleoceanography, 30, 317–331, https://doi.org/10.1002/2014PA002639, 2015.

Iwasaki, S., Kimoto, K., Okazaki, Y., and Ikehara, M.: Micro-CT Scanning of Tests of Three Planktic Foraminiferal Species to Clarify Dissolution Process and Progress, Geochem Geophys Geosyst, 20, 6051–6065, https://doi.org/10.1029/2019GC008456, 2019a.

Iwasaki, S., Kimoto, K., Sasaki, O., Kano, H., and Uchida, H.: Sensitivity of planktic foraminiferal test bulk density to ocean acidification, Sci Rep, 9, 9803, https://doi.org/10.1038/s41598-019-46041-x, 2019b.

Iwasaki, S., Lembke-Jene, L., Nagashima, K., Arz, H. W., Harada, N., Kimoto, K., and Lamy, F.: Evidence for late-glacial oceanic carbon redistribution and discharge from the Pacific Southern Ocean, Nat Commun, 13, 6250, https://doi.org/10.1038/s41467-022-33753-4, 2022.

Iwasaki, S., Kimoto, K., and Kucera, M.: Development of a Deep-Water Carbonate Ion Concentration Proxy Based on Preservation of Planktonic Foraminifera Shells Quantified by X-Ray CT Scanning, Paleoceanog and Paleoclimatol, 38, e2022PA004601, https://doi.org/10.1029/2022PA004601, 2023.

James, D. H., Bradbury, H. J., Antler, G., Steiner, Z., Hutchings, A. M., Sun, X., Saar, R., Greaves, M., and Turchyn, A. V.: Assessing Sedimentary Boundary Layer Calcium Carbonate Precipitation and Dissolution Using the Calcium Isotopic Composition of Pore Fluids, Front. Earth Sci., 9, 601194, https://doi.org/10.3389/feart.2021.601194, 2021.

Jana, D., Torres, M., Evans, K., Jayan, A. K., and Thirumalai, K.: Paired X-Ray Micro CT Scanning and Individual Foraminifera Isotopic Analysis Reveal (De)coupled Changes in Carbonate Preservation and Temperature, Paleoceanog and Paleoclimatol, 39, e2023PA004821, https://doi.org/10.1029/2023PA004821, 2024.

Johnstone, H. J. H., Schulz, M., Barker, S., and Elderfield, H.: Inside story: An X-ray computed tomography method for assessing dissolution in the tests of planktonic foraminifera, Marine Micropaleontology, 77, 58–70, https://doi.org/10.1016/j.marmicro.2010.07.004, 2010.

Johnstone, H. J. H., Yu, J., Elderfield, H., and Schulz, M.: Improving temperature estimates derived from Mg/Ca of planktonic foraminifera using X-ray computed tomography–based dissolution index, XDX, Paleoceanography, 26, 2009PA001902, https://doi.org/10.1029/2009PA001902, 2011.

Johnstone, H. J. H., Kiefer, T., Elderfield, H., and Schulz, M.: Calcite saturation, foraminiferal test mass, and Mg/Ca-based temperatures dissolution corrected using XDX—A 150 ka record from the western Indian Ocean, Geochem Geophys Geosyst, 15, 781–797, https://doi.org/10.1002/2013GC004994, 2014.

Jong, B. -J., Lo, L., Iizuka, Y., Shen, C. -C., Chuang, C. -K., Bahr, A., Mii, H. -S., Li, H. -C., and Löwemark, L.: Diagenetic Effect on Planktic Foraminiferal Mg/Ca Records in the Arctic Ocean, Geochem Geophys Geosyst, 27, e2025GC012302, https://doi.org/10.1029/2025GC012302, 2026.

Jonkers, L., Buse, B., Brummer, G.-J. A., and Hall, I. R.: Chamber formation leads to Mg/Ca banding in the planktonic foraminifer *Neogloboquadrina pachyderma*, Earth and Planetary Science Letters, 451, 177–184, https://doi.org/10.1016/j.epsl.2016.07.030, 2016.

Jung, S. J. A.: Radiocarbon age determinations on sediment core GIK23415-9., https://doi.org/10.1594/PANGAEA.186490, 2004.

Kim, S.-T. and O'Neil, J. R.: Equilibrium and nonequilibrium oxygen isotope effects in synthetic carbonates, Geochimica et Cosmochimica Acta, 61, 3461–3475, https://doi.org/10.1016/S0016-7037(97)00169-5, 1997.

Kozdon, R., Ushikubo, T., Kita, N. T., Spicuzza, M., and Valley, J. W.: Intratest oxygen isotope variability in the planktonic foraminifer N. pachyderma: Real vs. apparent vital effects by ion microprobe, Chemical Geology, 258, 327–337, https://doi.org/10.1016/j.chemgeo.2008.10.032, 2009.

Kubota, K., Yokoyama, Y., Ishikawa, T., Sagawa, T., Ikehara, M., and Yamazaki, T.: Equatorial Pacific seawater pCO2 variability since the last glacial period, Sci Rep, 9, 13814, https://doi.org/10.1038/s41598-019-49739-0, 2019.

Kucera, M.: Chapter Six Planktonic Foraminifera as Tracers of Past Oceanic Environments, in: Developments in Marine Geology, vol. 1, edited by: Hillaire-Marcel, C. and De Vernal, A., Elsevier, 213–262, https://doi.org/10.1016/S1572-5480(07)01011-1, 2007.

Kunioka, D., Shirai, K., Takahata, N., Sano, Y., Toyofuku, T., and Ujiie, Y.: Microdistribution of Mg/Ca, Sr/Ca, and Ba/Ca ratios in *Pulleniatina obliquiloculata* test by using a NanoSIMS: Implication for the vital effect mechanism, Geochem Geophys Geosyst, 7, 2006GC001280, https://doi.org/10.1029/2006GC001280, 2006.

Lauvset, S. K., Key, R. M., Olsen, A., van Heuven, S. M. A. C., Velo, A., Lin, X., Schirnick, C., Kozyr, A., Tanhua, T., Hoppema, M., Jutterström, S., Steinfeldt, R., Jeansson, E., Ishii, M., Pérez, F. F., Suzuki, T., and Watelet, S.: A new global interior ocean mapped climatology: the 1° × 1° GLODAP version 2 from 1972-01-01 to 2013-12-31 (NCEI Accession 0286118), https://doi.org/10.3334/CDIAC/OTG.NDP093_GLODAPV2, 2023.

Le, J. and Shackleton, N. J.: Carbonate dissolution fluctuations in the Western Equatorial Pacific during the Late Quaternary, Paleoceanography and Paleoclimatology, 7, 21–42, 1992.

Lewis, E. and Wallace, D. W. R.: Program Developed for $CO_2$ System Calculations, 1998.

Lohmann, G. P.: A model for variation in the chemistry of planktonic foraminifera due to secondary calcification and selective dissolution, Paleoceanography, 10, 445–457, https://doi.org/10.1029/95PA00059, 1995.

Lombard, F., Labeyrie, L., Michel, E., Spero, H. J., and Lea, D. W.: Modelling the temperature dependent growth rates of planktic foraminifera, Marine Micropaleontology, 70, 1–7, https://doi.org/10.1016/j.marmicro.2008.09.004, 2009.

Lueker, T. J., Dickson, A. G., and Keeling, C. D.: Ocean pCO2 calculated from dissolved inorganic carbon, alkalinity, and equations for K1 and K2: validation based on laboratory measurements of CO2 in gas and seawater at equilibrium, Marine Chemistry, 70, 105–119, https://doi.org/10.1016/S0304-4203(00)00022-0, 2000.

Manno, C., Morata, N., and Bellerby, R.: Effect of ocean acidification and temperature increase on the planktonic foraminifer *Neogloboquadrina pachyderma* (sinistral), Polar Biol, 35, 1311–1319, https://doi.org/10.1007/s00300-012-1174-7, 2012.

Martin, W. R. and Sayles, F. L.: $CaCO_3$ dissolution in sediments of the Ceara Rise, western equatorial Atlantic, Geochimica et Cosmochimica Acta, 60, 243–263, 1996.

Moffa-Sánchez, P., Hall, I. R., Barker, S., Thornalley, D. J. R., and Yashayaev, I.: Surface changes in the eastern Labrador Sea around the onset of the Little Ice Age, Paleoceanography, 29, 160–175, https://doi.org/10.1002/2013PA002523, 2014.

Morley, A., Babila, T. L., Wright, J., Ninnemann, U., Kleiven, K., Irvali, N., and Rosenthal, Y.: Environmental Controls on Mg/Ca in *Neogloboquadrina incompta* : A Core-Top Study From the Subpolar North Atlantic, Geochem Geophys Geosyst, 18, 4276–4298, https://doi.org/10.1002/2017GC007111, 2017.

Morley, A., De La Vega, E., Raitzsch, M., Bijma, J., Ninnemann, U., Foster, G. L., Chalk, T. B., Meilland, J., Cave, R. R., Büscher, J. V., and Kucera, M.: A solution for constraining past marine Polar Amplification, Nat Commun, 15, 9002, https://doi.org/10.1038/s41467-024-53424-w, 2024.

Nørgaard-Pedersen, N., Spielhagen, R. F., Erlenkeuser, H., Grootes, P., Heinemeier, J., and Knies, J.: Arctic Ocean during the Last Glacial Maximum: Atlantic and polar domains of surface water mass distribution and ice cover, Paleoceanography and Paleoclimatology, 18, https://doi.org/10.1029/2002PA000781, 2003.

Nyland, B. F., Jansen, E., Elderfield, H., and Andersson, C.: *Neogloboquadrina pachyderma* (dex. and sin.) Mg/Ca and $\delta^{18}$O records from the Norwegian Sea, Geochem Geophys Geosyst, 7, 2005GC001055, https://doi.org/10.1029/2005GC001055, 2006.

Olsen, A., Key, R. M., Van Heuven, S., Lauvset, S. K., Velo, A., Lin, X., Schirnick, C., Kozyr, A., Tanhua, T., Hoppema, M., Jutterström, S., Steinfeldt, R., Jeansson, E., Ishii, M., Pérez, F. F., and Suzuki, T.: The Global Ocean Data Analysis Project version 2 (GLODAPv2) – an internally consistent data product for the world ocean, Earth Syst. Sci. Data, 8, 297–323, https://doi.org/10.5194/essd-8-297-2016, 2016.

Petit, J. R., Jouzel, J., Raynaud, D., Barkov, N. I., Delaygue, G., Delmotte, M., Kotlyakov, V. M., Legrand, M., Lipenkov, V. Y., Lorius, C., Saltzmank, E., and Stievenard, M.: Climate and atmospheric history of the past 420,000 years from the Vostok ice core, Antarctica, 1999.

Procter, F. A., Piazolo, S., John, E. H., Walshaw, R., Pearson, P. N., Lear, C. H., and Aze, T.: Electron backscatter diffraction analysis unveils foraminiferal calcite microstructure and processes of diagenetic alteration, Biogeosciences, 21, 1213–1233, https://doi.org/10.5194/bg-21-1213-2024, 2024.

Rahmstorf, S., Box, J. E., Feulner, G., Mann, M. E., Robinson, A., Rutherford, S., and Schaffernicht, E. J.: Exceptional twentieth-century slowdown in Atlantic Ocean overturning circulation, Nature Clim Change, 5, 475–480, https://doi.org/10.1038/nclimate2554, 2015.

Rassmann, J., Lansard, B., Pozzato, L., and Rabouille, C.: Carbonate chemistry in sediment porewaters of the Rhône River delta driven by early diagenesis (northwestern Mediterranean), Biogeosciences, 13, 5379–5394, https://doi.org/10.5194/bg-13-5379-2016, 2016.

Reuning, L., Reijmer, J. J. G., Betzler, C., Swart, P., and Bauch, T.: The use of paleoceanographic proxies in carbonate periplatform settings—opportunities and pitfalls, Sedimentary Geology, 175, 131–152, https://doi.org/10.1016/j.sedgeo.2004.12.026, 2005.

Rosenthal, Y., Bova, S., and Zhou, X.: A User Guide for Choosing Planktic Foraminiferal Mg/Ca-Temperature Calibrations, Paleoceanog and Paleoclimatol, 37, e2022PA004413, https://doi.org/10.1029/2022PA004413, 2022.

Roza-Llera, A., Di Lorenzo, F., Churakov, S. V., Jiménez, A., and Fernández-Díaz, L.: Pb Removal Efficiency by Calcium Carbonates: Biogenic versus Abiogenic Materials, Crystal Growth & Design, 24, 79–92, https://doi.org/10.1021/acs.cgd.3c00517, 2024.

Russell, A. D., Hönisch, B., Spero, H. J., and Lea, D. W.: Effects of seawater carbonate ion concentration and temperature on shell U, Mg, and Sr in cultured planktonic foraminifera, Geochimica et Cosmochimica Acta, 68, 4347–4361, https://doi.org/10.1016/j.gca.2004.03.013, 2004.

Sadekov, A. Yu., Eggins, S. M., and De Deckker, P.: Characterization of Mg/Ca distributions in planktonic foraminifera species by electron microprobe mapping, Geochem Geophys Geosyst, 6, 2005GC000973, https://doi.org/10.1029/2005GC000973, 2005.

Saenger, C. P. and Evans, M. N.: Calibration and Validation of Environmental Controls on Planktic Foraminifera Mg/Ca Using Global Core-Top Data, Paleoceanog and Paleoclimatol, 34, 1249–1270, https://doi.org/10.1029/2018PA003507, 2019.

Sejrup, H. P., Haflidason, H., and Andrews, J. T.: A Holocene North Atlantic SST record and regional climate variability, Quaternary Science Reviews, 30, 3181–3195, https://doi.org/10.1016/j.quascirev.2011.07.025, 2011.

Spero, H. J. and Lea, D. W.: Experimental determination of stable isotope variability in *Globigerina bulloides*: implications for paleoceanographic reconstructions, Marine Micropaleontology, 28, 231–246, https://doi.org/10.1016/0377-8398(96)00003-5, 1996.

Spindler, M. and Dieckmann, G. S.: Distribution and abundance of the planktic foraminifer *Neogloboquadrina pachyderma* in sea ice of the Weddell Sea (Antarctica), Polar Biol, 5, 185–191, https://doi.org/10.1007/BF00441699, 1986.

Thunell, R. C.: Calcium carbonate dissolution history in late quaternary deep-sea sediments, Western Gulf of Mexico, Quaternary Research, 6, 281–297, 1976.

Tierney, J. E., Malevich, S. B., Gray, W., Vetter, L., and Thirumalai, K.: Bayesian Calibration of the Mg/Ca Paleothermometer in Planktic Foraminifera, Paleoceanog and Paleoclimatol, 34, 2005–2030, https://doi.org/10.1029/2019PA003744, 2019.

Turchyn, A. V., Bradbury, H. J., Walker, K., and Sun, X.: Controls on the Precipitation of Carbonate Minerals Within Marine Sediments, Front. Earth Sci., 9, 618311, https://doi.org/10.3389/feart.2021.618311, 2021.

Uppström, L. R.: The boron/chlorinity ratio of deep-sea water from the Pacific Ocean, Deep Sea Research and Oceanographic Abstracts, 21, 161–162, https://doi.org/10.1016/0011-7471(74)90074-6, 1974.

Van Der Land, C., Mienis, F., De Haas, H., Frank, N., Swennen, R., and Van Weering, T. C. E.: Diagenetic processes in carbonate mound sediments at the south-west Rockall Trough margin: Diagenetic processes in carbonate mound sediments, Sedimentology, 57, 912–931, https://doi.org/10.1111/j.1365-3091.2009.01125.x, 2010.

Van Raden, U. J., Groeneveld, J., Raitzsch, M., and Kucera, M.: Mg/Ca in the planktonic foraminifera *Globorotalia inflata* and *Globigerinoides bulloides* from Western Mediterranean plankton tow and core top samples, Marine Micropaleontology, 78, 101–112, https://doi.org/10.1016/j.marmicro.2010.11.002, 2011.

Westgård, A., Ezat, M. M., Chalk, T. B., Chierici, M., Foster, G. L., and Meilland, J.: Large-scale culturing of *Neogloboquadrina pachyderma* , its growth in, and tolerance of, variable environmental conditions, Journal of Plankton Research, 45, 732–745, https://doi.org/10.1093/plankt/fbad034, 2023.

Westgård, A., Ezat, M. M., Sykes, F. E., Meilland, J., Chalk, T. B., Milton, J. A., Chierici, M., and Foster, G. L.: Extending planktic foraminiferal Mg/Ca palaeothermometry into polar temperature ranges: crust- and lamellae specific calibrations and non-thermal controls, https://doi.org/10.5194/egusphere-2026-2415, 6 May 2026.

Yu, J. and Elderfield, H.: Benthic foraminiferal B/Ca ratios reflect deep water carbonate saturation state, Earth and Planetary Science Letters, 258, 73–86, https://doi.org/10.1016/j.epsl.2007.03.025, 2007.

Zamelczyk, K., Fransson, A., Chierici, M., Jones, E., Meilland, J., Anglada-Ortiz, G., and Lødemel, H. H.: Distribution and Abundances of Planktic Foraminifera and Shelled Pteropods During the Polar Night in the Sea-Ice Covered Northern Barents Sea, Front. Mar. Sci., 8, 644094, https://doi.org/10.3389/fmars.2021.644094, 2021.

Zarkogiannis, S. D., Kontakiotis, G., Gkaniatsa, G., Kuppili, V. S. C., Marathe, S., Wanelik, K., Lianou, V., Besiou, E., Makri, P., and Antonarakou, A.: An Improved Cleaning Protocol for Foraminiferal Calcite from Unconsolidated Core Sediments: HyPerCal—A New Practice for Micropaleontological and Paleoclimatic Proxies, JMSE, 8, 998, https://doi.org/10.3390/jmse8120998, 2020.

Zarkogiannis, S. D., Iwasaki, S., Rae, J. W. B., Schmidt, M. W., Mortyn, P. G., Kontakiotis, G., Hertzberg, J. E., and Rickaby, R. E. M.: Calcification, Dissolution and Test Properties of Modern Planktonic Foraminifera From the Central Atlantic Ocean, Front. Mar. Sci., 9, 864801, https://doi.org/10.3389/fmars.2022.864801, 2022.

Zeebe, R. E.: History of Seawater Carbonate Chemistry, Atmospheric $CO_2$, and Ocean Acidification, Annu. Rev. Earth Planet. Sci., 40, 141–165, https://doi.org/10.1146/annurev-earth-042711-105521, 2012.

Zeebe, R. E. and Wolf-Gladrow, D.: $CO_2$ in Seawater: Equilibrium, Kinetics, Isotopes, Elsevier, Amsterdam, 346 pp., 2001.